



Long-range intramolecular allostery and regulation in the dynein-like AAA protein Mdn1

Keith J. Mickolajczyk^a, Paul Dominic B. Olinares^b, Yiming Niu^c, Nan Chen^a, Sara E. Warrington^a, Yusuke Sasaki^d, Thomas Walz^c, Brian T. Chait^b, and Tarun M. Kapoor^{a,1}

^aLaboratory of Chemistry and Cell Biology, The Rockefeller University, New York, NY 10065; ^bLaboratory of Mass Spectrometry and Gaseous Ion Chemistry, The Rockefeller University, New York, NY 10065; ^cLaboratory of Molecular Electron Microscopy, The Rockefeller University, NY 10065; and ^dTri-Institutional Therapeutics Discovery Institute, New York, NY 10065

Edited by Edwin W. Taylor, The University of Chicago, Chicago, IL, and approved June 25, 2020 (received for review February 13, 2020)

Mdn1 is an essential mechanoenzyme that uses the energy from ATP hydrolysis to physically reshape and remodel, and thus mature, the 60S subunit of the ribosome. This massive (>500 kDa) protein has an N-terminal AAA (ATPase associated with diverse cellular activities) ring, which, like dynein, has six ATPase sites. The AAA ring is followed by large (>2,000 aa) linking domains that include an ~500-aa disordered (D/E-rich) region, and a C-terminal substrate-binding MIDAS domain. Recent models suggest that intramolecular docking of the MIDAS domain onto the AAA ring is required for Mdn1 to transmit force to its ribosomal substrates, but it is not currently understood what role the linking domains play, or why tethering the MIDAS domain to the AAA ring is required for protein function. Here, we use chemical probes, single-particle electron microscopy, and native mass spectrometry to study the AAA and MIDAS domains separately or in combination. We find that Mdn1 lacking the D/E-rich and MIDAS domains retains ATP and chemical probe binding activities. Free MIDAS domain can bind to the AAA ring of this construct in a stereo-specific bimolecular interaction, and, interestingly, this binding reduces ATPase activity. Whereas intramolecular MIDAS docking appears to require a treatment with a chemical inhibitor or preribosome binding, bimolecular MIDAS docking does not. Hence, tethering the MIDAS domain to the AAA ring serves to prevent, rather than promote, MIDAS docking in the absence of inducing signals.

midasin | dynein | AAA ATPase | ribosome biogenesis

Proteins in the AAA superfamily, which includes ~100 members in humans, are responsible for a diversity of mechanochemical activities in the cell, ranging from protein quality control to intracellular transport (1–5). Many AAA members self-assemble into homohexameric rings and use the energy from ATP hydrolysis to thread protein substrates through their central pores (1, 6). Two notable exceptions are the microtubule-based motor protein dynein and the ribosome biogenesis factor Mdn1 (also known as midasin, or Rea1 in *Saccharomyces cerevisiae*), each of which have six AAA domains, together with additional domains, expressed tandemly on a single polypeptide (7). While the mechanistic divergence of dynein from other AAA proteins has been established (8), relatively little is known about Mdn1. Current models speculate that dynein and Mdn1 may share common mechanisms of action, but more work is needed to examine Mdn1 biochemistry for proper comparisons with dynein mechanochemistry.

The overall domain structure of Mdn1, which is 4,717 amino acids (aa) long in *Schizosaccharomyces pombe*, has been defined from genomic and structural studies (7, 9, 10). From its N terminus, Mdn1 has a short (130 aa) N domain followed by its six AAA subunits, then >2,000 aa of linking domains, and finally a C-terminal MIDAS (metal ion-dependent adhesion site) domain. Like dynein, the six AAA domains are arranged in a ring. Unlike dynein, all six AAA sites in Mdn1 can bind ATP, and current data suggest that four (AAA2–5) hydrolyze ATP (11). The remaining domains in Mdn1 do not bear homology to dynein. The linking domains subdivide into a mainly helical region

termed the linker, which folds into an ~20-nm-long extended structure in *S. pombe*, followed by the ~500-aa D/E-rich region, which is proposed to be unstructured (9, 10). The MIDAS domain has homology to the integrin I domain (7, 12), and has been shown to bind ribosomal assembly factors (13, 14). It is not currently understood how these domains coordinate their functions, or why it is necessary for them all to be present on a single polypeptide.

While advanced models are available for how ATP hydrolysis is coupled to domain motions in dynein (8), less is known about Mdn1. Nonetheless, structural studies have provided evidence that long-range, intramolecular docking of MIDAS domain onto the AAA ring may play a role in the Mdn1 mechanochemical cycle (9, 10). The cryo-EM structure of Mdn1 in the presence of AMP-PNP revealed no density for the MIDAS domain and approximately half of the linking domains (9). Similarly, MIDAS docking was not observed by EM in multiple nucleotide states for wild-type *S. cerevisiae* Mdn1/Rea1 (10). However, in the presence of the potent, Mdn1-selective chemical probe Rbin-1 (11), the MIDAS domain docked onto AAA3/4 (9). MIDAS docking was also observed in a mutant of *S. cerevisiae* Mdn1 in which the helix 2 insert of AAA2 was removed (10). These two methods of

Significance

The dynein-like AAA motor Mdn1 drives ribosome biogenesis by using ATP-fueled motions to dislodge assembly factor proteins from 60S precursor particles. It is not known how this unusually large (>500 kDa) mechanoenzyme coordinates the activities of its C-terminal MIDAS domain, which binds specific preribosomal proteins, with the ATPase cycle in its N-terminal AAA ring. Here, we show that the linking domains, which include a >500-amino acid disordered region, regulate an intramolecular binding interaction between the AAA and MIDAS domains. Surprisingly, the linking domains down-regulate MIDAS-AAA binding despite tethering these two domains together. This study provides insights into the regulation of Mdn1 function and into the design principles of large, multidomain mechanoenzymes.

Author contributions: K.J.M. and T.M.K. conceived and designed the project; K.J.M. and S.E.W. made plasmids and purified proteins; K.J.M. ran biochemical assays and analyses; P.D.B.O. performed native mass spectrometry experiments with supervision by B.T.C.; K.J.M. and Y.N. prepared negative-stain EM grids and performed data analysis with supervision by T.W.; N.C. assisted with photo-crosslinking experiments and analyses; Y.S. synthesized Rbin-XL; and K.J.M. and T.M.K. wrote the manuscript with contributions from all other authors.

The authors declare no competing interest.

This article is a PNAS Direct Submission.

Published under the PNAS license.

Data deposition: Maps were deposited to Electron Microscopy Data Bank (<https://www.ebi.ac.uk/pdbe/emdb/>) in entries EMD-21911 and EMD-21912.

¹To whom correspondence may be addressed. Email: kapoor@rockefeller.edu.

This article contains supporting information online at <https://www.pnas.org/lookup/suppl/doi:10.1073/pnas.2002792117/-DCSupplemental>.

First published July 21, 2020.

inducing MIDAS docking had contrasting effects on ATPase activity: Deleting the helix 2 insert of AAA2 increased the ATPase rate of Mdn1 ~10-fold, whereas addition of Rbin-1 inhibited the ATPase activity (9, 10). The interplay between MIDAS binding and ATPase activity in the AAA ring thus remains an open question.

The MIDAS-docked conformation induced by Rbin-1 structurally mimics the preribosome-bound form of Mdn1 (9). Mdn1 is known to play an essential role in the maturation of the 60S ribosomal subunit (11, 13), where it binds other assembly factors via its MIDAS domain and has been proposed to use ATP-powered motions to physically dislodge them (14–18). Cryo-EM studies of pre-60S particles have shown that the MIDAS domain is docked for Mdn1/Real1 within these large multicomponent complexes (9, 12, 16). Here the MIDAS domain is simultaneously bound to both the AAA ring and the assembly factor protein, providing a direct path of force transmission from the motor domains to the assembly factors that are being removed. These structural data thus suggest that Mdn1 docks its MIDAS domain when it engages the pre-60S particle, removes the assembly factor, then undocks its MIDAS domain and disengages from the pre-60S particle such that it can recycle. However, this model suggests that the linking domains are little more than a passive tether, making it difficult to explain why they have remained relatively well-conserved (7)—and why the AAA ring and MIDAS domain have remained on the same polypeptide—throughout eukaryotic evolution. It may be expected that tethering the MIDAS domain serves to favor docking by increasing local concentration, but this hypothesis has not been tested.

In the current work, we investigate the role of the linking domains in the MIDAS docking cycle and the overall mechanism of Mdn1. Using recombinant proteins, we reconstitute MIDAS docking as a bimolecular interaction between separately expressed AAA and MIDAS domains. Whereas for full-length Mdn1 MIDAS docking (unimolecular) must be induced by the addition of Rbin-1, untethered (bimolecular) MIDAS docking is Rbin-1-independent with submicromolar affinity. Hence, quite the opposite of the expected effect of increasing local concentration, tethering the MIDAS domain negatively regulates docking. The separately expressed AAA ring can bind ATP and Rbin-1 similarly to the full-length protein, but Rbin-1 binding does not inhibit ATPase activity. Interestingly, inhibition can instead be induced by the addition of free MIDAS. Altogether, our results suggest that the linking domains are a regulatory element that prevents MIDAS docking in the absence of inducing signals, such as Rbin-1 treatment or preribosome binding, and that MIDAS docking negatively regulates ATPase activity in the AAA ring.

Results

Free MIDAS Protein Binds to Truncated Mdn1 Lacking a MIDAS Domain.

To investigate the role of the linking domains in Mdn1, we first asked if intramolecular docking of the MIDAS domain onto the AAA ring could be reconstituted as a two-protein interaction (Fig. 1A). We thus designed a streptavidin-Dynabead pull-down assay using *S. pombe* Mdn1 lacking the D/E-rich and MIDAS regions (hereafter Mdn1- Δ C, amino acids 1 to 3,911) as “prey” and MIDAS domain with an N-terminal biotinylated SNAP tag as “bait” (Fig. 1B). Both full-length Mdn1 (Mdn1-FL) and Mdn1- Δ C were expressed in insect cells with an N-terminal His-tag and purified using affinity, ion-exchange, and size-exclusion chromatography (Methods). Typical preparations yielded ~0.05 mg of these very large proteins (~540 and 450 kDa for Mdn1-FL and Mdn1- Δ C, respectively) per liter of insect cells. Purity and relative size of the proteins were assessed by SDS/PAGE and by size-exclusion chromatography, where each protein eluted as a single peak (SI Appendix, Fig. S1 A–C).

The MIDAS domain was expressed in bacteria as an N-terminal SNAP-tag fusion (hereafter WT-MIDAS), which we found aided in expression and ease of purification. The construct also included an N-terminal His-tag, which was removed by protease treatment during the purification protocol (affinity, ion-exchange, and size-exclusion chromatography; Methods). In addition to WT-MIDAS, we also made a SNAP-tagged construct lacking the conserved “MIDAS loop” (hereafter Δ Loop-MIDAS), which has been shown to be required for docking onto the Mdn1 AAA ring (Fig. 1B) (12). Typical yields were in excess of 2 mg of purified protein per liter of cultured bacteria. Purity of the MIDAS constructs were assessed by SDS/PAGE and size-exclusion chromatography (SI Appendix, Fig. S1 D and E). MIDAS constructs were biotinylated via the SNAP-tag (Methods) prior to size-exclusion chromatography (SI Appendix, Fig. S1F).

We ran the pull-down assays in the presence of the small-molecule inhibitor Rbin-1 (1 μ M), as this compound is required to induce MIDAS docking in Mdn1-FL (9). We found that WT-MIDAS (1 μ M) at a 15-fold molar excess pulled down $67 \pm 7\%$ (mean \pm SD) of Mdn1- Δ C (65 nM input). The empty beads and Δ Loop-MIDAS (1 μ M) each pulled down 10% or less (Fig. 1 C and D), indicating no significant specific binding. Together, these data indicate that the MIDAS docking interaction can be reconstituted as a two-protein interaction, hereafter referred to as untethered docking.

Untethered MIDAS Docking Structurally Matches Tethered MIDAS Docking.

We next asked if there was a stereotyped position on the Mdn1- Δ C AAA ring where free MIDAS would dock. To address this question, we performed negative-stain EM imaging of Mdn1- Δ C together with WT-MIDAS at a 1:10 molar ratio (25 and 250 nM, respectively) in the presence of Rbin-1 (1 μ M). Raw images revealed monodisperse molecules of Mdn1- Δ C with a characteristic ladle-like appearance, as well as multiple small particles corresponding to the smaller MIDAS proteins (SI Appendix, Fig. S2 A and B).

We collected ~13,000 particles and subjected them to 2D and 3D classifications followed by supervised 3D classification using as references the resolution-filtered cryo-EM structures of Mdn1-FL in AMP-PNP and ATP + Rbin-1 (PDB ID codes 6OR5 and 6ORB, respectively) (9). This method yielded two density maps, each at ~25-Å resolution (Fig. 1 E–G and SI Appendix, Fig. S2C). Map 1 contained most of the particles (~63%), and allowed for identification of the linker domain, AAA ring, and central pore. The top surface of the AAA ring, viewed with the linker facing upward, appeared relatively flat (Fig. 1E). Map 2, which corresponded to the remaining particles (~37%), had additional density on the top surface of the AAA ring (Fig. 1F). Map 1 was aligned with map 2, and a difference map was generated. This analysis revealed that the additional density of map 2 appeared on the top surface of the AAA ring opposite the linker (Fig. 1G). No major changes in the linker domain were observed within the allowance of ~25-Å resolution.

To check if the extra density corresponded to the MIDAS domain, we docked the previously determined models of Mdn1-FL in the presence of AMP-PNP (where the MIDAS domain was not seen to dock onto the Mdn1 ring) and in presence of ATP + Rbin-1 (where the MIDAS domain was seen to dock onto the Mdn1 ring) (9) into Map 2 (Fig. 1H; additional views in SI Appendix, Fig. S2D). We found that the extra density was not accounted for by the AMP-PNP model, but was accounted for by the MIDAS domain (shown in red) in the ATP + Rbin-1 model. Hence, untethered docking occurs with 1:1 stoichiometry and at the position in Mdn1-FL expected from structural models for tethered docking. This result demonstrates that stereo-specific MIDAS docking does not require a tethered connection between the AAA and MIDAS domains.

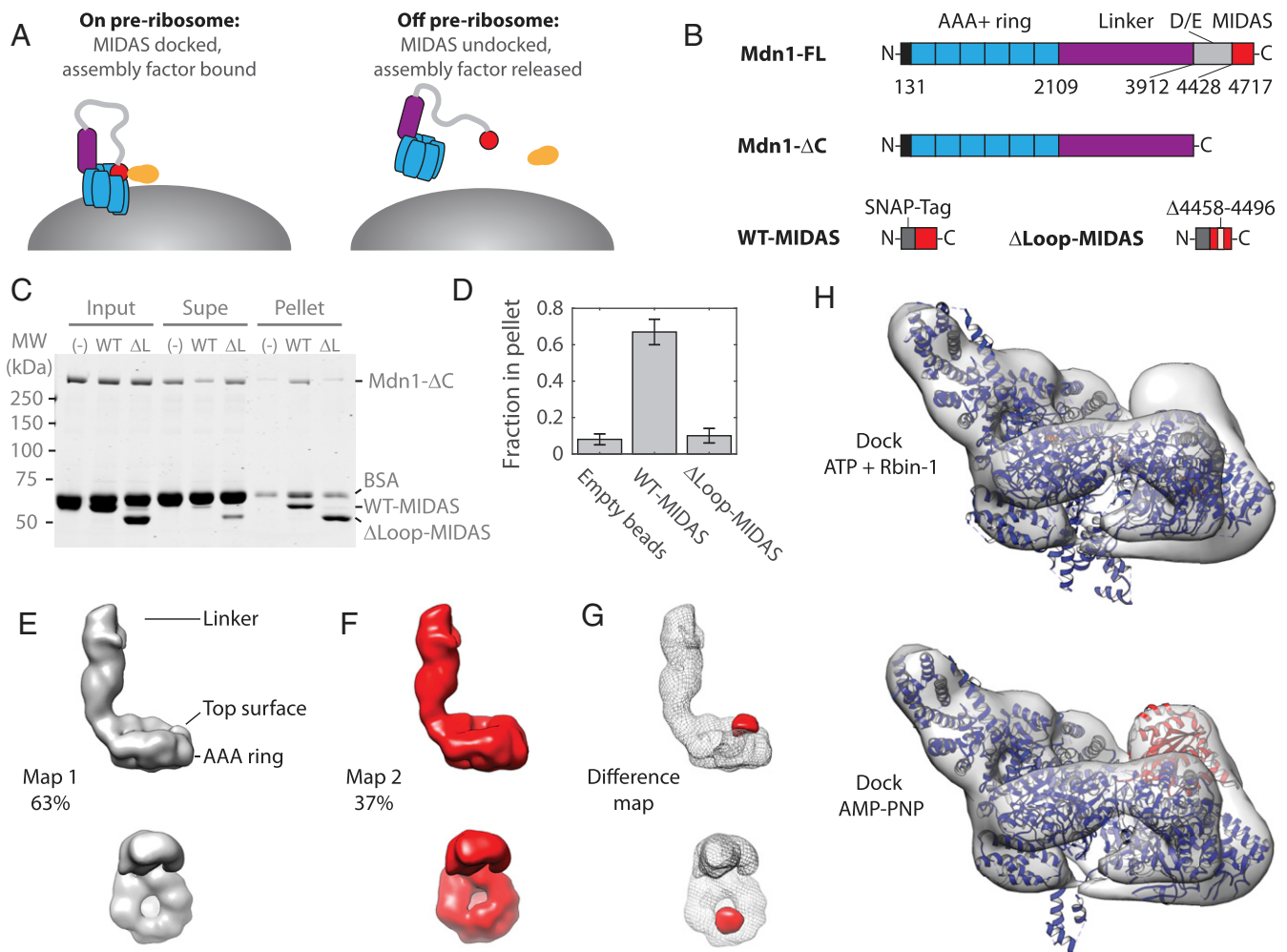


Fig. 1. Direct binding of separately expressed MIDAS protein to truncated Mdn1. (A) Diagram showing major conformational changes in Mdn1. Upon binding to the preribosome particle (dark gray), Mdn1 docks its MIDAS domain (red) onto the AAA ring (light blue). The MIDAS domain simultaneously binds to an assembly factor (orange), which it dislodges from the preribosome. Illustration is not to scale. (B) Diagram showing position of domains in Mdn1 full-length (FL) and ΔC , as well as the SNAP-tagged MIDAS domain. Color coding of domains matches A. The linker and D/E-rich regions make up the linking domains. Numbers denote start of domains. (C) Example SDS/PAGE gel (Coomassie stain) of input, supernatant (supe), and pellet of Mdn1- ΔC prey (65 nM) pulled down with no MIDAS (-), wild-type MIDAS (WT), or Δ Loop-MIDAS (ΔL) bait (1 μ M). Bait was biotinylated via the SNAP tag and adhered to streptavidin-coated dynabeads. All experiments contain 1 μ M Rbin-1. (D) Fraction of total Mdn1- ΔC pelleted by empty beads, WT-MIDAS, or Δ Loop-MIDAS. Data shown as mean \pm SD for $n = 3$ independent experiments with at least 2 separate preps of each protein. (E) Density map 1 obtained with particles from negative-stain EM imaging of the bimolecular docking interaction (25 nM Mdn1- ΔC , 250 nM SNAP-MIDAS, 1 μ M Rbin-1). Map thresholded at 5 SD from the mean. (F) Density map 2. Map 2 was resampled onto map 1 and thresholded at 5 SD from the mean. (G) Difference map (red, thresholded at 20 SD from mean) superimposed on map 1. (H) Docking previously determined Mdn1-FL AMP-PNP (PDB ID code 6OR5) and ATP+Rbin-1 (PDB ID code 6ORB) models into negative-stain EM density map 2. The expected position of the MIDAS domain (red) maps to the extra density present in map 2 (EMDB ID code EMD-21912) but not map 1 (EMDB ID code EMD-21911). Additional information is provided in *SI Appendix, Figs. S1 and S2*.

Untethered MIDAS Docking Is Rbin-1-Independent. For wild-type Mdn1-FL in solution, significant docking of the MIDAS domain has not been seen unless Rbin-1 is present (9). Furthermore, tethering two domains should increase the effective concentration to promote binding. We therefore reasoned that the untethered docking reaction between Mdn1- ΔC and WT-MIDAS should be a low-affinity, Rbin-1-dependent interaction (Fig. 2A). To examine this, we first ran a pull-down assay in the absence of Rbin-1. We expected to see very little Mdn1- ΔC get pulled down. Surprisingly, we saw the opposite. Running the pull-down with just a 15-fold excess of WT-MIDAS bait to Mdn1- ΔC prey (1 μ M to 65 nM), we were able to pull down ~65% (Fig. 2B), similar to the amount pulled down in the presence of Rbin-1 (Fig. 1D).

To investigate the Rbin-1-dependence of untethered docking in more detail, we reran the pull-down assay at the same protein concentrations, but varied the Rbin-1 concentration. We found that the pelleted fraction was independent of the Rbin-1 concentration, with approximately equal fractions pulled down over a wide range (0 to 5 μ M) of Rbin-1 concentrations (Fig. 2C and D and *SI Appendix, Fig. S2E*). Hence, in these reaction conditions, untethered docking is not sensitive to Rbin-1.

To estimate the strength of the untethered docking interaction, we next ran a titration pull-down using various concentrations of MIDAS-WT bait (0–1 μ M to 65 nM Mdn1- ΔC prey) in the absence of Rbin-1. We observed an increase in the fraction of Mdn1- ΔC bound with increasing concentration of WT-MIDAS, although we were not able to achieve a complete (100%)

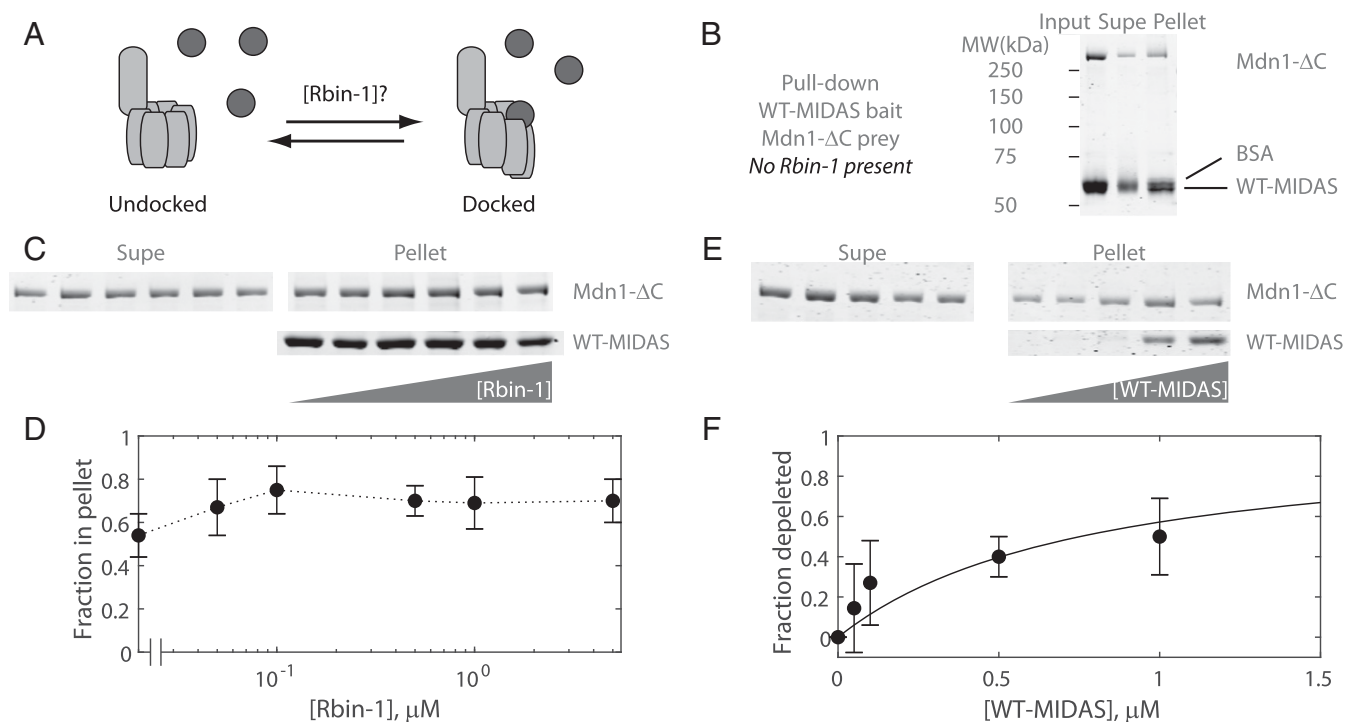


Fig. 2. Linking domains are required for the regulation of MIDAS docking. (A) Diagram showing that Rbin-1 may regulate formation of the untethered (bimolecular) docked conformation. Mdn1- Δ C is shown in light gray, and WT-MIDAS is shown in dark gray. Illustration is not to scale. (B) Example pull-down of Mdn1- Δ C prey (65 nM) with WT-MIDAS bait (1 μ M) with no Rbin-1 present. (C) Example pull-down of Mdn1- Δ C prey (65 nM) with WT-MIDAS bait (1 μ M) at Rbin-1 concentrations ranging from 0 to 5 μ M. Full gel is shown in *SI Appendix, Fig. S2E*. (D) Quantification of pull-down experiment shown in C. Data shown as mean \pm SD for $n = 3$ independent experiments. Dotted line connects data points to guide the eye. (E) Example pull-down of Mdn1- Δ C prey (65 nM) with no Rbin-1 present and various concentrations of WT-MIDAS bait (0 to 1 μ M). Full example gels are shown in *SI Appendix, Fig. S2F*. (F) Quantification of Mdn1- Δ C depletion from the supernatant at various concentrations of WT-MIDAS bait, corresponding to E. Data shown as mean \pm SD for $n = 3$ independent experiments and fitted to a hyperbola (*Methods*) to estimate the dissociation constant ($K_D = 0.72 \pm 0.58 \mu\text{M}$). Fit weighted by inverse SEM. Gels in B, C, and E analyzed by SDS/PAGE (Coomassie stain).

pull-down (Fig. 2 E and F and *SI Appendix, Fig. S2F*). We posit this incomplete pull-down is due to the large size or nucleotide state of Mdn1- Δ C. Nonetheless, we were able to analyze the dissociation constant by fitting a hyperbola to the fraction of Mdn1- Δ C depleted from the supernatant. We estimated a tight, submicromolar dissociation constant ($K_D = 0.72 \pm 0.58 \mu\text{M}$, fit \pm 95% CI). Hence, untethered docking is a surprisingly high-affinity bimolecular interaction and, contrasting the case of tethered docking, does not require Rbin-1. Together, the data in Fig. 2 do not support a model in which the linking domains serve to increase the local concentration of MIDAS, and instead point to the possibility that they serve to prevent MIDAS docking in the absence of Rbin-1.

Mdn1-FL and Mdn1- Δ C Have Similar ATPase Activities. Why is untethered docking Rbin-1-independent while tethered docking is Rbin-1-dependent? To address this question, we next sought to characterize the biochemical properties of Mdn1- Δ C relative to Mdn1-FL. We first ran steady-state ATPase assays on Mdn1-FL and Mdn1- Δ C as a function of ATP concentration to test for cooperativity between the six AAA domains and to assess affinities and turnover rates. We found that the ATPase rates for Mdn1-FL could be fit by a Michaelis-Menten model, with a k_{cat} of $2.4 \pm 0.2 \text{ s}^{-1}$ and a K_M of $0.25 \pm 0.05 \mu\text{M}$ (fit \pm 95% CI; Fig. 3A and *SI Appendix, Fig. S3*). These values are close to those of other AAA proteins such as spastin (19). Expanding the fit to a Hill model returned a Hill coefficient within error of unity, indicating a lack of cooperativity in ATP binding and hydrolysis

(*SI Appendix, Fig. S3*). These results contrast with other AAA proteins such as ClpXP (20, 21), which have Hill coefficients larger than unity. The ATPase activity of Mdn1- Δ C was similar to that of Mdn1-FL under our experimental conditions, with a k_{cat} of $2.6 \pm 0.2 \text{ s}^{-1}$ and K_M of $0.53 \pm 0.08 \mu\text{M}$ (Fig. 3A). Hence, the ATP hydrolysis properties of the Mdn1 AAA ring do not appear to be impacted by truncating off the MIDAS domain.

Mdn1- Δ C Can Bind ADP at All Sites and Exchange AMP-PNP at Multiple Sites. We next investigated the nucleotide binding in Mdn1- Δ C using native mass spectrometry (MS). We first characterized Mdn1- Δ C prepared in nucleotide-free buffer prior to native MS analysis (*Methods*). The mass spectrum revealed three distinct peaks corresponding to masses larger than the expected molecular weight of apo Mdn1- Δ C (Fig. 3B and *SI Appendix, Table S1*). The lowest measured peak was $\sim 1,800 \text{ Da}$ above the molecular weight of apo Mdn1- Δ C, and each subsequent peak was $\sim 450 \text{ Da}$ larger (Fig. 3B). Since Mg-ADP has a molecular weight of 451.5 Da, we assigned three peaks to be Mdn1- Δ C with four, five, and six molecules of Mg-ADP bound, consistent with the six ATP-binding sites in Mdn1 (Fig. 3C). Further supporting this interpretation, removing the N-terminal His-tag of Mdn1- Δ C with a protease caused an equal and predictable shift in mass for all three peaks (*SI Appendix, Fig. S4*).

The majority of the Mdn1- Δ C protein had five Mg-ADP bound, but a fractional population had six Mg-ADP bound. We hence wondered if we could shift weight from the four- and five-Mg-ADP-bound peaks into the six-Mg-ADP-bound peak by

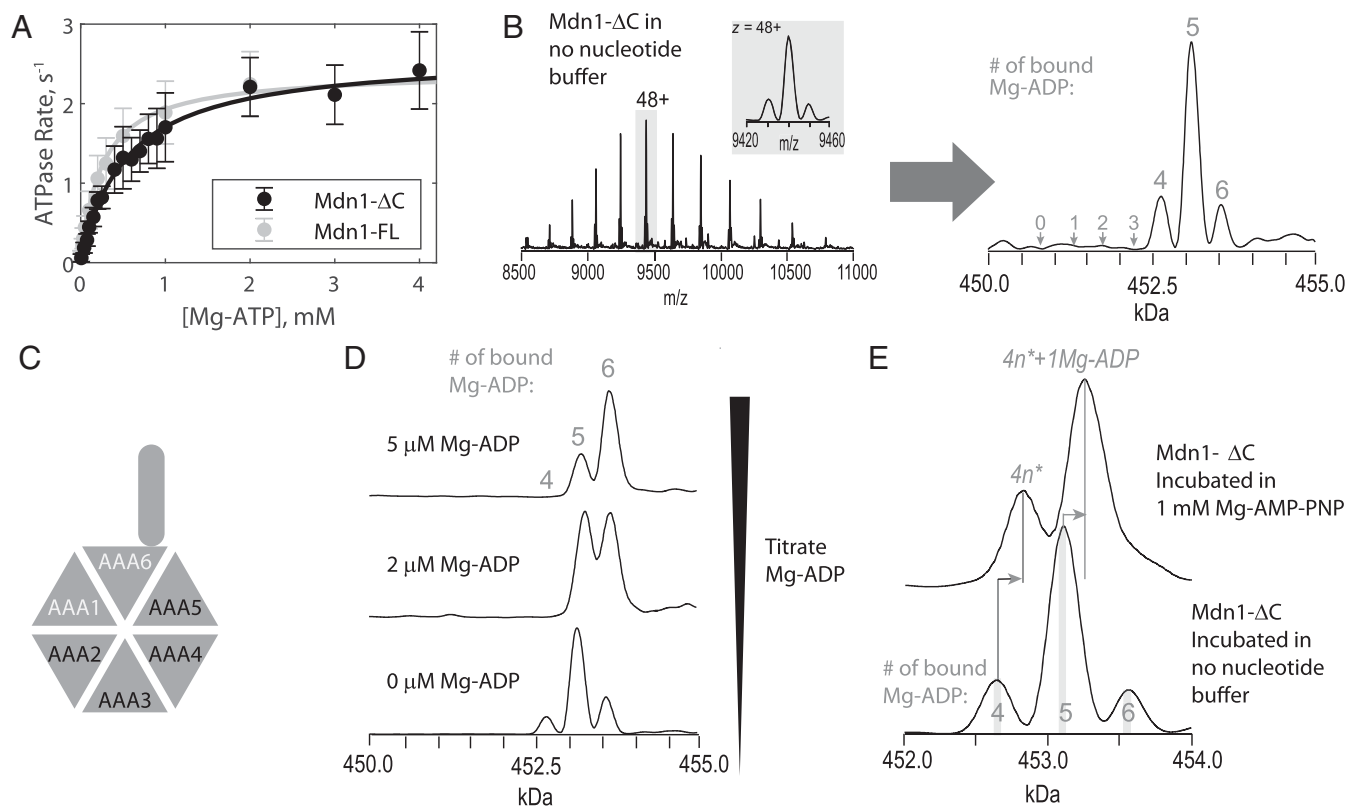


Fig. 3. Comparison of the biochemical properties of Mdn1-FL and Mdn1- Δ C. (A) ATPase activity as a function of ATP concentration for Mdn1-FL ($n = 6$ to 8 measurements from 2 to 3 separate protein preparations) and Mdn1- Δ C ($n = 3$ to 7 from 2 to 3 separate protein preparations). Data shown as mean \pm SD. Fits to Michaelis-Menten equation (solid lines) weighted by inverse SEM. (B) Mass spectrum of Mdn1- Δ C (inset shows zoomed-in region) prepared with no nucleotide present before and after charge-state deconvolution. Gray numbers depict the number of Mg-ADP molecules bound, with 0 denoting the mass of apo Mdn1- Δ C (SI Appendix, Table S1, shows mass assignments). (C) Diagram highlighting the ATPase-competence of AAA modules in Mdn1. All six modules have ATP binding motifs, but only AAA-2-5 (black font) have motifs required for ATP hydrolysis. (D) Deconvolved mass spectra of Mdn1- Δ C (1.5 μ M) incubated with increasing concentrations of Mg-ADP. (E) Deconvolved mass spectra of Mdn1- Δ C incubated with 1 mM Mg-AMP-PNP prior to buffer exchange compared to apo. Designation n^* indicates a combined number of AMP-PNP and ADP nucleotides.

adding Mg-ADP to the MS analysis buffer. Indeed, we saw that addition of low micromolar amounts of Mg-ADP substantially shifted the amounts of Mdn1- Δ C to higher masses with up to six bound Mg-ADP (Fig. 3D). At the highest Mg-ADP condition (5 μ M), the majority of Mdn1- Δ C had six Mg-ADP bound. Hence, it is possible to fill all six nucleotide pockets in Mdn1- Δ C with ADP.

We next prepared Mdn1- Δ C with 1 mM Mg-AMP-PNP prior to exchange into MS analysis buffer. In this sample, we saw only two peaks, each shifted toward slightly heavier mass than the nucleotide-free sample (Fig. 3E). The difference in mass between these two peaks again corresponded to the molecular weight of Mg-ADP. The mass of the lower peak could correspond to two AMP-PNP plus two ADP or three AMP-PNP plus one ADP, depending on the number of magnesium ions bound (SI Appendix, Table S1). Hence the major peak likely corresponds to Mdn1- Δ C with five nucleotides bound. While attaining mass spectra for Mdn1-FL proved difficult, likely due to the disordered and highly charged D/E-rich region, we note that we previously observed five nucleotides bound to Mdn1-FL in the cryo-EM structure determined in the presence of AMP-PNP (9). Based on these native mass spectrometry data for Mdn1- Δ C and EM data for Mdn1-FL, we speculate that these constructs have similar nucleotide-binding characteristics. Only three or fewer subunits in Mdn1- Δ C exchanged from ADP into AMP-PNP

under our experimental conditions. As a point of comparison, cytoplasmic dynein exchanges AMP-PNP at three, or possibly all four, of its nucleotide-binding-competent AAA modules (22, 23). Together, these data indicate that truncating off the D/E-rich and MIDAS domain does not substantially alter the biochemical activity of Mdn1, and that Rbin-1-independent docking of free WT-MIDAS on Mdn1- Δ C is therefore not likely due to differences between Mdn1-FL and Mdn1- Δ C nucleotide binding or hydrolysis. We note that additional experiments are going to be needed to more firmly establish this.

Mdn1- Δ C Can Bind Rbin-XL. Treatment of Mdn1-FL with the small molecule inhibitor Rbin-1 structurally mimics the pre-60S ribosomal subunit-bound conformation (9). While Rbin-1 treatment is required for tethered docking, it is not required for untethered docking. We hence asked if Rbin-1 can bind to or inhibit Mdn1- Δ C. To test for inhibitor binding, we used the available structure-activity relationship data (11) to design a Rbin-1 analog that incorporates both a diazirine group for photo-cross-linking and an alkyne group for click chemistry (Fig. 4A). We synthesized this analog (SI Appendix, Supplemental Text), which we named Rbin-XL, and found that it inhibited Mdn1-FL in an ATPase assay (EC_{50} of 0.23 ± 0.33 μ M, fit \pm 95% CI), validating its use (Fig. 4B and SI Appendix, Fig. S5A). We reasoned that, if the Rbin-1-independence of untethered MIDAS docking stems

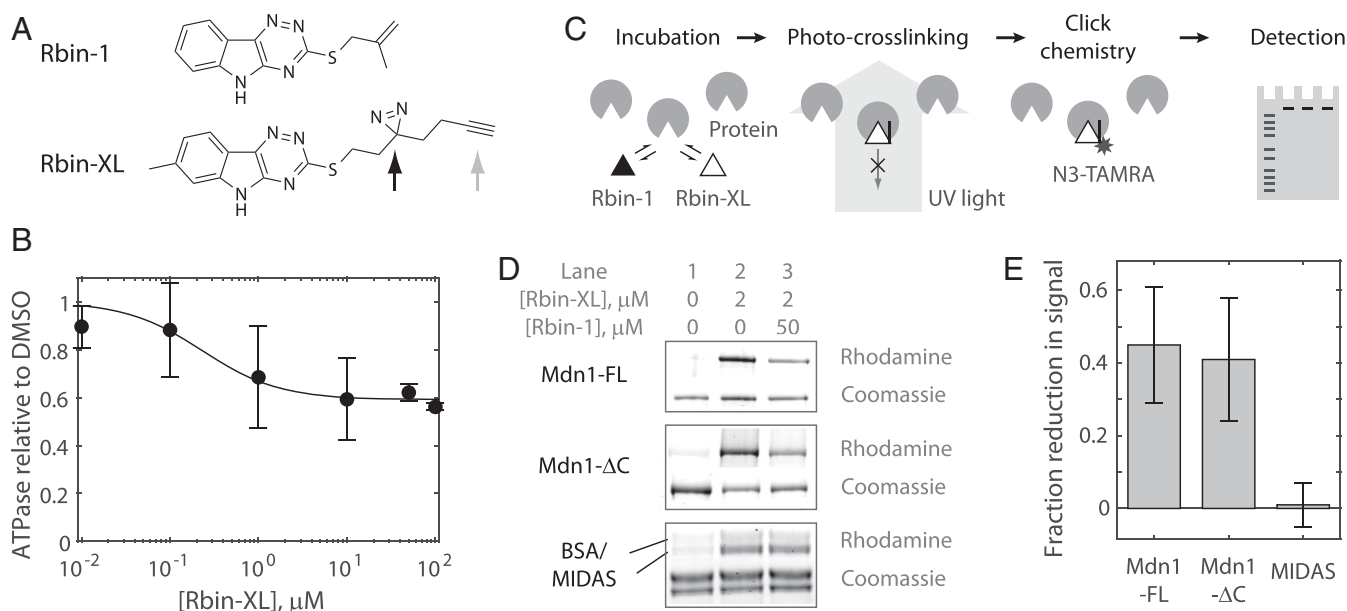


Fig. 4. Rbin compounds can bind to Mdn1- ΔC . (A) Chemical structures of Rbin-1 and the UV-cross-linkable analog Rbin-XL. The diazirine group (black arrow) in Rbin-XL enables UV-cross-linking, and the alkyne (gray arrow) enables click chemistry-mediated attachment of rhodamine. (B) Mdn1-FL ATPase as a function of Rbin-XL concentration. Each data point shows mean \pm SD for $n = 4$ to 5 measurements from 2 to 3 separate preparations. Data were normalized to DMSO control and fitted to a sigmoidal dose-response equation with Y-offset. Similar partial inhibition of ATPase activity is also seen for other Rbin analogs (11). (C) Schematic illustrating the workflow for the detection of photo-cross-linking probes. In an initial incubation step, Rbin-1 can displace noncovalently bound Rbin-XL. Treatment with UV light leads to the formation of a covalent bond between Rbin-XL and the target protein. Protein-bound Rbin-XL can subsequently be labeled with a fluorescent dye and analyzed by SDS/PAGE. (D) Example gels showing the rhodamine and Coomassie signals for the designated proteins of interest subsequent to UV-cross-linking of Rbin-XL and attachment of rhodamine azide via click chemistry. A decrease in the ratio of rhodamine-to-Coomassie signal upon addition of Rbin-1 indicates specific binding of Rbin-XL. (E) Fraction reduction in the rhodamine-to-Coomassie signal in the Rbin-1-added lane relative to the Rbin-XL-alone lane. Data shown as mean \pm SD for $n = 3$ to 4 measurements from at least 2 separate protein preparations.

from differences in the Mdn1- ΔC AAA ring, Rbin-XL binding might be abrogated.

To test for Rbin-XL binding, we performed a competition binding assay employing Rbin-XL and Rbin-1 (Fig. 4C). Mdn1 constructs were mixed with either Rbin-XL alone (2 μM) or with Rbin-XL and a 25-fold molar excess of Rbin-1 and incubated on ice in the dark for 30 min. We then initiated Rbin-XL cross-linking by exposure to UV light, followed by click-chemistry-mediated attachment of rhodamine to the Rbin-XL alkyne. Finally, we ran SDS/PAGE and measured the ratio of rhodamine signal to Coomassie signal. A decrease in this ratio in the Rbin-1-added lane relative to the Rbin-XL-alone lane indicates binding of Rbin-XL prior to the photo-cross-linking process that can be competed off by Rbin-1. For Mdn1-FL, we indeed saw a robust decrease in signal in the Rbin-1-added lane relative to the Rbin-XL-alone lane (Fig. 4D and E and *SI Appendix*, Fig. S5B). We saw a similar signal decrease for Mdn1- ΔC , providing evidence for specific binding of Rbin compounds. We also note cross-linking to BSA, visible as rhodamine signal. As incubation with Rbin-1, prior to UV exposure, does not suppress the signal, we interpret this as nonspecific cross-linking of Rbin-XL with BSA (blocking agent). Nonspecific binding can also account for the partial suppression of signal in the Mdn1 lanes (Fig. 4E). We also analyzed WT-MIDAS protein (Fig. 1B) and saw no competition, indicating that Rbin compounds do not specifically bind to the MIDAS domain in isolation. A lack of binding between WT-MIDAS and Rbin-1 was also observed in native MS (*SI Appendix*, Fig. S6). Overall, these results provide evidence that Rbin compounds can bind to Mdn1-FL and Mdn1- ΔC , but not to WT-MIDAS domain alone.

Mdn1- ΔC Is Not Inhibited by Rbin-1. Given that Rbin compounds bind to Mdn1- ΔC , we expected that they would inhibit activity in an ATPase assay. We thus ran steady-state ATPase assays at saturating amounts of ATP and titrated Rbin-1 concentrations for both Mdn1-FL and Mdn1- ΔC . Mdn1-FL showed a dose-dependent response, with an EC_{50} of $0.14 \pm 0.12 \mu\text{M}$ and a lower plateau value of 0.37 ± 0.07 (fit \pm 95% CI; Fig. 5A). A nonzero lower plateau is consistent with previous characterizations of Rbin analogs (11). We note that the difference in lower plateaus between Rbin-1 (Fig. 5A) and Rbin-XL (Fig. 4B) may indicate some degradation of Rbin-XL during the ATPase assay. Contrasting expectation, Mdn1- ΔC ATPase activity showed no response to Rbin-1, even at very high (100 μM) concentrations. Similar to Rbin-1, Rbin-XL did not inhibit Mdn1- ΔC in our assay conditions (*SI Appendix*, Fig. S5A). Hence, Rbin compounds can bind to Mdn1- ΔC without inhibiting it, indicating that the C-terminal domains are required for coupling compound binding to functional inhibition.

The decoupling of Rbin-1 binding and inhibition in Mdn1- ΔC suggests that the chemical inhibitor does not directly interfere with ATP binding, but rather works through an allosteric mechanism that requires the MIDAS domain. To test for an allosteric mechanism, we performed ATPase competition assays with Rbin-1 using Mdn1-FL. We found that the addition of 1 μM Rbin-1 reduces the k_{cat} but not the K_{M} ($2.1 \pm 0.2 \text{ s}^{-1}$ vs. $1.1 \pm 0.2 \text{ s}^{-1}$ and $0.20 \pm 0.04 \mu\text{M}$ vs. $0.24 \pm 0.09 \mu\text{M}$ for DMSO control and 1 μM Rbin-1 conditions, respectively) of ATP-dependent Mdn1-FL ATPase activity (Fig. 5B and C). Hence, Rbin-1 inhibition of Mdn1-FL is noncompetitive, consistent with an allosteric mechanism. Together with the data in Fig. 4, these data

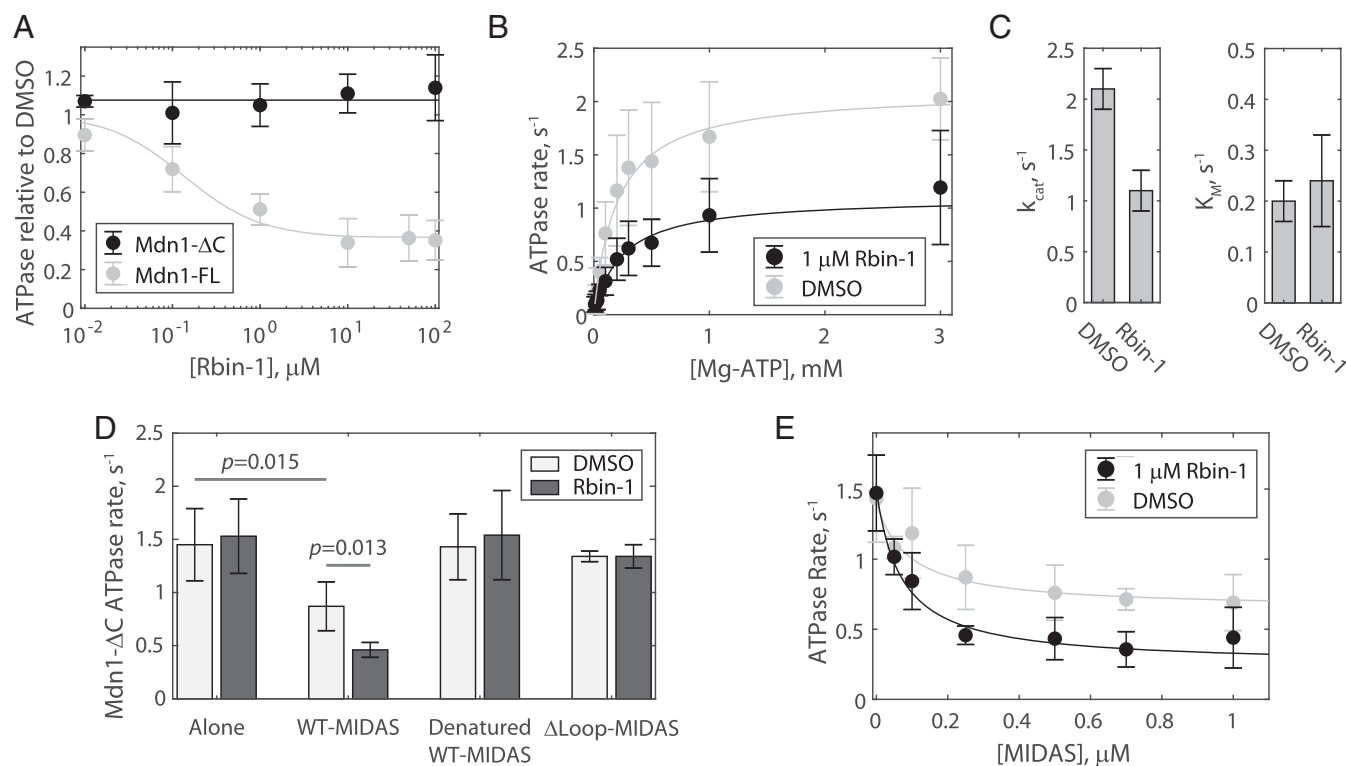


Fig. 5. Untethered MIDAS docking reduces the ATPase activity of Mdn1- Δ C. (A) Concentration-dependent inhibition of Rbin-1 on Mdn1-FL and Mdn1- Δ C ATPase rates. Data were normalized to DMSO control. Mdn1-FL data were fitted to a sigmoidal dose-response equation with Y-offset. For Mdn1- Δ C, the mean value across conditions is shown to guide the eye. All data points show mean \pm SD for $n = 4$ to 5 measurements from 2 to 3 separate preparations. (B) ATPase activity as a function of ATP concentration for Mdn1-FL with or without Rbin-1 (1 μ M) present ($n = 3$ measurements from 3 separate protein preparations). Data shown as mean \pm SD. Fits to Michaelis-Menten equation (solid lines) weighted by inverse SEM. (C) Fitted constants from C shown as fit \pm 95% CI. (D) ATPase rate of Mdn1- Δ C (25 nM) in the presence of 250 nM of the stated MIDAS constructs both with (dark gray bars) and without (light gray bars) Rbin-1 (1 μ M). All data shown as mean \pm SD for $n = 3$ to 4 independent measurements including at least 2 separate preparations of each protein used. Statistical significance was measured using an unpaired Student's t test. (E) Dose-response curve of Mdn1- Δ C ATPase activity in the presence (black) or absence (gray) of Rbin-1 (1 μ M) at various concentrations of free WT-MIDAS ($n = 3$ to 5 independent measurements). Fitting to a hyperbolic model that decreases to maximum inhibition revealed that Rbin-1 had little effect on the EC_{50} (0.09 ± 0.13 μ M and 0.06 ± 0.07 μ M for DMSO and Rbin-1, respectively), but reduced the lower plateau value (0.65 ± 0.21 s^{-1} and 0.32 ± 0.26 s^{-1} for DMSO and Rbin-1, respectively).

suggest that Mdn1- Δ C can bind, but cannot be inhibited by, Rbin-1.

Binding of Free MIDAS Protein Reduces the ATPase Rate of Mdn1- Δ C.

Given that chemical inhibitor binding is insufficient for ATPase inhibition of Mdn1- Δ C (Figs. 4 and 5 A–C), we next asked if MIDAS docking, in the absence of Rbin-1, could lead to inhibition. We thus ran steady-state ATPase assays with Mdn1- Δ C and free WT-MIDAS. We found that the addition of WT-MIDAS to Mdn1- Δ C (250 nM to 25 nM, matching the stoichiometry used in the negative-stain EM experiments; Fig. 1 E–H) reduced the ATPase rate nearly twofold (Fig. 5D). Addition of heat-denatured WT-MIDAS or Δ Loop-MIDAS (similarly at 250 nM) did not significantly decrease the ATPase rate of Mdn1- Δ C. Hence, the ability of a given MIDAS construct to influence the ATPase rate of Mdn1- Δ C correlated with its ability to bind to it (Figs. 1D and 5D).

We next ran the same experiment in the presence of Rbin-1. While Rbin-1 did not inhibit Mdn1- Δ C alone, it did lead to further inhibition when Mdn1- Δ C was mixed with WT-MIDAS (Fig. 5D). No decrease was seen when WT-MIDAS was denatured before use or when Δ Loop-MIDAS was used. These results show that the MIDAS domain is required for inhibition by Rbin-1.

We next measured the Mdn1- Δ C ATPase rate as we titrated the WT-MIDAS concentration with no Rbin-1 present. We observed dose-response inhibitory behavior that plateaued at high WT-MIDAS concentrations (Fig. 5E). The EC_{50} measured here (0.09 ± 0.13 μ M) serves as an upper-limit estimate of the K_D for the MIDAS docking interaction: the exact mechanism of inhibition for MIDAS-driven ATPase inhibition is unknown, but for common models (i.e., noncompetitive, mixed inhibition, etc.), $K_I \leq EC_{50}$ (24). This estimate supports the submicromolar dissociation constant estimated from pull-down assays (Fig. 2F). The ATPase plateauing at a nonzero value (0.65 ± 0.21 s^{-1}) resembles the result seen for titrating Rbin-1 on Mdn1-FL (Fig. 5A); indeed, both plateaued at $\sim 40\%$ of their initial value. When we ran this assay with Rbin-1 present, we measured a further maximum inhibition (0.32 ± 0.26 s^{-1}), but with an EC_{50} within error of the DMSO value (0.06 ± 0.07 μ M; Fig. 5E). The similar EC_{50} values provide a second line of evidence that Rbin-1 does not significantly alter the binding affinity of Mdn1- Δ C to WT-MIDAS. However, even small changes in the EC_{50} could indicate mixed inhibition, and further experiments are needed to examine this. Altogether, these data provide evidence that MIDAS docking, tethered or untethered, in and of itself is sufficient to inhibit Mdn1 ATPase activity, with Rbin-1 providing further fractional inhibition.

Discussion

In this study, we assay the roles of the linking domains in the AAA protein Mdn1, a critical component of the ribosome biogenesis machinery. We find that the linking domains serve to prevent MIDAS docking onto the AAA ring in the absence of Rbin-1 treatment or preribosome binding. Moreover, MIDAS docking negatively regulates ATPase activity in the AAA ring. These results provide insights into the design principles of Mdn1 and of large, multidomain AAA proteins in general.

How might the Mdn1 linker and D/E-rich region serve to regulate the docking of the MIDAS domain onto the AAA ring? One possibility is that the lengths of these domains are finely tuned such that the MIDAS domain can only reach the AAA ring when the protein is in a specific conformation or state of flexibility. Both the linker and D/E-rich domains are large, and tend to scale in size with one another in different organisms (7, 9). For *S. pombe*, the D/E-rich region is 517 amino acids long, and the distance from the end of the linker to the docking position is ~ 24 nm (9). To gain insight into whether the lengths and mechanics of the linking regions may play a role in limiting tethered MIDAS docking, we ran a simple Brownian dynamics simulation. We modeled the D/E-rich region as a worm-like chain and used a Monte Carlo approach to simulate tethered diffusion of the MIDAS domain (Fig. 6A). We find that extending the D/E-rich region such that the MIDAS could dock would introduce ~ 1.3 pN of intramolecular tension (Fig. 6A and B). Furthermore, we find that the MIDAS domain only spends $\sim 0.02\%$ of its time within 2 nm of the docking site (Fig. 6C). Although this model is very simple, as it ignores volume exclusions and attractive potentials, it raises the possibility that the relative sizes of the linker domain and D/E-rich tethers may underlie the inefficiencies of tethered MIDAS docking. It furthermore emphasizes how changes to the structure or overall flexibility of the linker domain, particularly at the hinge point (a point of proposed flexibility in the linker; ref. 9; Fig. 6C), may substantially alter MIDAS docking dynamics. A second possibility, which we do not favor, is that the negatively charged ($pI = 3.7$) D/E-rich region physically sequesters the MIDAS domain while in specific conformations. Further functional and structural studies of Mdn1 will be needed to test these and other potential models.

Several multimeric AAA proteins such as Yme1 (25), katanin (26, 27), and numerous others (28) are thought to hydrolyze ATP in a sequential rotary fashion. Mdn1 is unlikely to function in such a way because (i) only four of the six AAA modules in Mdn1 can hydrolyze ATP (11); (ii) Rbin-1 can bind to, but cannot inhibit, Mdn1- ΔC (Figs. 4 and 5A); and (iii) inhibition by Rbin-1 or MIDAS is partial (Fig. 5A and E). Mdn1 further differs from canonical AAA proteins in that it does not show positive cooperativity in its ATPase activity (Fig. 3A), and in that its binding partner (the MIDAS domain) inhibits, rather than activates, ATPase activity (5). Mdn1 may instead divide labor among its AAA domains, similar to dynein (8, 22, 29–31).

Our results also provide insights into the mechanisms by which Rbin compounds inhibit Mdn1. Partial inhibition of Mdn1 ATPase has been seen previously for Rbin compounds ($\sim 40\%$) (11). Even Mdn1 with a Walker B mutation in AAA5, which has an ATPase rate nearly 10-fold lower than wild-type, is partially inhibited ($\sim 50\%$) by Rbin-1 (9). Rbin-1 treatment also induces tethered MIDAS docking in Mdn1-FL (9). Here we find that both of these effects occur independent of Rbin-1 when separately expressed WT-MIDAS protein is mixed with Mdn1- ΔC (Figs. 2 and 5D and E). We also find by Rbin-XL binding experiments (Fig. 4) and by ATPase assays with both WT-MIDAS and Rbin-1 present (Fig. 5D and E) that Rbin-1 can bind to Mdn1- ΔC . However, without MIDAS present, Rbin-1 cannot inhibit Mdn1- ΔC (Fig. 5A). Taken altogether, these results argue

against the possibility that Rbin-1 works exclusively on the AAA ring. Instead, we propose that Rbin-1 works by relieving the regulatory effects of the linking domains. Rbin-1 may enable tethered MIDAS docking, which in turn inhibits Mdn1-FL ATPase. In support of this allosteric mechanism, we find that Rbin-1 is a noncompetitive inhibitor of Mdn1-FL (Fig. 5B and C). The two-step inhibition of Mdn1- ΔC by MIDAS and Rbin-1 may indicate a mixed mechanism for the separated proteins, or potentially separate effects on two or more of the active ATPase sites.

Mdn1 may not follow the canonical AAA mechanism of threading substrates through the central pore of its hexameric AAA ring (2). Here, we extend existing models (9, 10, 12, 15) to suggest that Mdn1 instead uses its MIDAS domain to (i) simultaneously bind to both an assembly factor and its own AAA ring, (ii) transmit information about substrate binding (mimicked by Rbin-1) to the AAA ring (Figs. 4 and 5), and (iii) transmit force produced in the AAA ring to the assembly factor. This MIDAS-mediated mechanism may be a more general alternative strategy utilized by a subclass of AAA proteins. One example is the MoxR-group AAA protein CbbQ, a Rubisco activase that requires a MIDAS-containing cofactor protein to function (32–34). Recent structural work has shown that the MIDAS-containing von Willebrand factor A (VWA) domain of this cofactor docks onto the hexameric AAA ring of CbbQ in a bimolecular interaction, and furthermore that the VWA domain

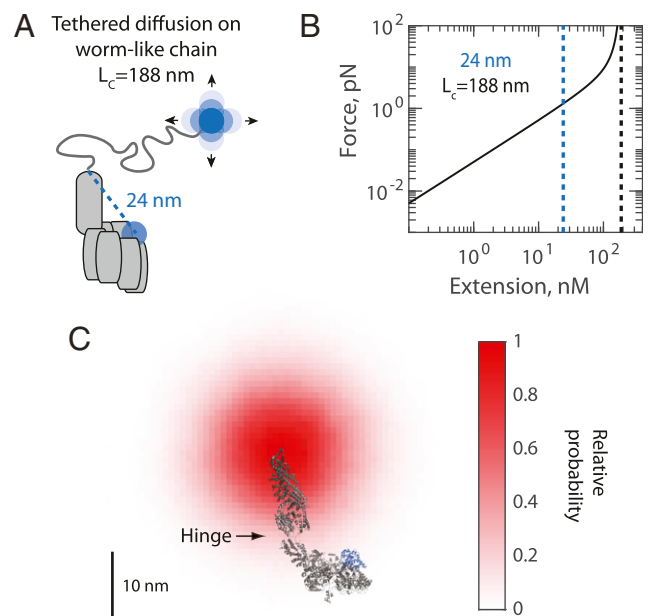


Fig. 6. Brownian dynamics simulations of tethered MIDAS diffusion. (A) The D/E-rich region can be modeled as a worm-like chain. The D/E-rich region has a contour length of 188 nm and its end-to-end distance must be ~ 24 nm to reach the MIDAS docking site. Diagram not to scale. (B) Force–extension curve for the Mdn1 D/E-rich region. Extending to reach the MIDAS docking position can lead to ~ 1.3 pN of intramolecular tension. Contour length (L_c) shown in red. (C) Diagram superimposing the probability density function of tethered MIDAS positions (D/E-rich region modeled as a worm-like chain) onto the cryo-EM structure (PDB ID code 6ORB) of Mdn1. Darker red colors indicate a higher probability of the end position of the D/E-rich region being at that location. Arrow denotes position of hinge, around which the linker may have some flexibility (9). Diagram to scale. The MIDAS domain (blue) reaches within 2 nm of its docking position in only 0.02% of simulated time points.

communicates information about substrate binding to the AAA ring (32). Other AAA proteins such as RavA, chelatase, and VWA8 either work with a MIDAS-containing cofactor or have a fused VWA domain (2, 35–39). We propose that the MIDAS-mediated mechanism is a general paradigm for some AAA proteins, and furthermore propose that keeping the MIDAS domain on the same polypeptide as the AAA domains, as opposed to in a cofactor protein, enables an additional level of regulation in Mdn1.

Together, our data shed light on the role of the linking domains in regulating the docking of the MIDAS domain onto the AAA ring. In contrast to the expectation that tethering the MIDAS domain might favor docking by increasing local concentration, we find that untethering the MIDAS domain leads to tight (submicromolar) binding that no longer requires Rbin-1. Regulation by these large linking domains provides insight into why Mdn1 has remained a single polypeptide, and one of the largest enzymes in the genome, throughout eukaryotic evolution. Long-range regulation between N- and C-terminal domains is also reminiscent of other ATPase enzymes such as kinesin (40, 41), dynein (42), and receptor tyrosine kinase (43).

Materials and Methods

Protein Expression and Purification. *S. pombe* Mdn1-FL and Mdn1- Δ C (amino acids 1 to 3,911) were cloned into pFastbac HTC (Thermo Fisher 10584027) and expressed in insect cells as previously reported (9, 11). Recombinant baculoviruses were generated using the Bac-to-Bac system (Thermo Fisher). High Five cells (Thermo Fisher B85502) were grown to ~3.0 million cells per milliliter in Express Five 5FM (Thermo Fisher 10486025) supplemented with antibiotic-antimycotic (Life Technologies 15240-062) and 16 mM L-glutamine (Life Technologies 25030-081) prior to infection with P2 viral stocks at a 1:50 virus:media ratio. Cells were cultured in suspension (27 °C, shaking at 115 rpm) for 48 h prior to harvesting.

Mdn1-FL and Mdn1- Δ C were purified using a modified version of a previously reported protocol (9, 11). All purification steps were carried out at 4 °C. Cells were lysed using a Dounce homogenizer (Thomas Scientific) in ~25 mL of lysis buffer (50 mM Tris [pH 7.5], 400 mM NaCl, 1 mM MgCl₂, 10% wt/vol glycerol, 20 mM imidazole, 5 mM 2-mercaptoethanol, 0.2 mM ATP, 1 mM PMSF, 3 U/mL Benzonase, 1× Roche complete protease inhibitor without EDTA) per liter of initial cell culture. The crude lysate was centrifuged at 55,000 rpm in a Type 70 Ti rotor (Beckman Coulter) for 1 h, then filtered using 0.22- μ m Millex-GP PES membrane filters (Millipore SLGP033RS). The clarified lysate was loaded onto a HisTrap FF Crude column (GE Life Sciences 29048631) preequilibrated with wash buffer (50 mM Tris [pH 7.5], 400 mM NaCl, 1 mM MgCl₂, 10% wt/vol glycerol, 20 mM imidazole, 5 mM 2-mercaptoethanol, 0.2 mM ATP). The column was washed with 25 mL wash buffer before elution with elution buffer (12.5 mM Tris [pH 7.5], 100 mM NaCl, 0.25 mM MgCl₂, 10% wt/vol glycerol, 300 mM imidazole, 1.25 mM 2-mercaptoethanol, 50 μ M ATP). The eluent was filtered and then loaded onto either a HiTrap Q HP column for Mdn1-FL (GE Life Sciences 29051325) or a MonoQ 5/50 GL column for Mdn1- Δ C (GE Life Sciences 17516601). The proteins were eluted on a gradient of low salt (20 mM Tris [pH 7.5], 100 mM NaCl, 1 mM MgCl₂, 10% wt/vol glycerol, 5 mM 2-mercaptoethanol, 0.2 mM ATP) and high salt buffers (low salt buffer with 1 M NaCl), and the relevant fractions were determined by SDS/PAGE. The pooled eluents were concentrated using a 100-kDa-cutoff Amicon Ultra-4 Centrifugal filter (Millipore UFC810009) and loaded onto a Superose 6 Increase 10/300 GL column (GE Life Sciences 29091596) in sizing buffer (20 mM Tris [pH 7.5], 150 mM NaCl, 1 mM MgCl₂, 0.5 mM EGTA, 3% wt/vol glycerol, 1 mM DTT, 50 μ M ATP). To allow for click chemistry, a Hepes-based sizing buffer was used (20 mM Hepes [pH 7.5], 150 mM NaCl, 1 mM MgCl₂, 3% wt/vol glycerol, 1 mM DTT). The eluent was concentrated to at least 0.2 mg/mL using 100-kDa-cutoff Amicon filters as above. Final protein concentration was determined using the colorimetric Bradford assay (Bio-Rad 5000006).

The SNAP-MIDAS construct was generated by subcloning Mdn1 aa 4,381 to 4,717 into pSNAP-tag(T7)-2 (NEB N91815) downstream of the SNAP tag. An N-terminal 6× His tag and a Tobacco Etch Virus (TEV) protease site were added upstream of the SNAP tag. For the Δ Loop-MIDAS construct, aa 4,458 to 4,496 were replaced with a GS linker. Cloning was verified by Sanger sequencing. Both MIDAS constructs were expressed and purified using the same protocol. MIDAS proteins were expressed in *Escherichia coli* Rosetta (DE3) pLysS cells (Merck 70954) grown in Miller's LB medium (Formedium LMM105). Expression was induced at A600 = 0.6 to 0.8 with 0.5 mM IPTG

(Goldbio), and the cultures were grown at 18 °C for 16 h. Cultures were pelleted and resuspended in lysis buffer (50 mM Hepes [pH 7.5], 150 mM NaCl, 1 mM MgCl₂, 10% wt/vol glycerol, 20 mM imidazole, 5 mM 2-mercaptoethanol, 1 mM PMSF, 3 U/mL Benzonase, 1× Roche complete protease inhibitor without EDTA). All purification steps were carried out at 4 °C. Cells were lysed using an Emulsiflex-C5 homogenizer (Avestin; four cycles at ~10,000 psi), and the crude lysate was centrifuged at 55,000 rpm in a Type 70 Ti rotor (Beckman Coulter) for 30 min. The supernatant was filtered through a 0.22- μ m Millex-GP PES membrane (Millipore SLGP033RS) and loaded onto a HisTrap HP column (GE Life Sciences 17-5247-01) preequilibrated with wash buffer (50 mM Hepes [pH 7.5], 150 mM NaCl, 1 mM MgCl₂, 10% wt/vol glycerol, 20 mM imidazole, 5 mM 2-mercaptoethanol). The column was washed with 25 mL of wash buffer and eluted with wash buffer plus 400 mM imidazole. The eluent was treated with His-tagged TEV protease (~0.1 mg/mL) and dialyzed against 1 L of dialysis buffer (20 mM Hepes [pH 7.5], 100 mM NaCl, 1 mM MgCl₂, 10% wt/vol glycerol, 20 mM imidazole, 5 mM 2-mercaptoethanol) for 3 h at 4 °C. His-TEV protease was removed by incubation on Ni-NTA resin (Qiagen) for 10 min. The supernatant was then loaded onto a HiTrap Q HP column (GE Life Sciences 29051325) and eluted over a gradient of low salt (same as dialysis buffer) and high salt (dialysis buffer with 1 M NaCl) buffers. Relevant fractions were located by SDS/PAGE, pooled, and concentrated using a 30-kDa-cutoff Amicon Ultra-4 centrifugal filter (Millipore UFC803008). Nonbiotinylated samples were immediately loaded onto a Superdex 200 Increase 10/300 GL column (GE Life Science 28990944) in sizing buffer (20 mM Hepes [pH 7.5], 150 mM NaCl, 1 mM MgCl₂, 3% wt/vol glycerol, 1 mM DTT). Biotinylated samples were mixed with SNAP-Biotin (NEB S91105) following the manufacturer-suggested protocol prior to sizing as above. Biotinylation was verified using the colorimetric HABA assay (Pierce 28005), and protein concentration was determined using the colorimetric Bradford assay (Bio-Rad 5000006).

NADH-Coupled Steady-State ATPase Assay. ATPase assays were carried out using time-course fluorescence measurements in a Synergy Neo Microplate reader (340 nm excitation, 440 nm emission) (9). All assays were carried out in Mdn1 assay buffer (20 mM Tris [pH 7.5], 150 mM NaCl, 1 mM MgCl₂, 0.5 mM EGTA, 1 mM DTT) supplemented with 200 μ M NADH (Sigma N7410), 1 mM phosphoenolpyruvic acid (Sigma P7127), 30 U/mL D-lactic dehydrogenase, and 30 U/mL pyruvate kinase (Sigma P1506). Unless otherwise stated, 1 mM of Mg-ATP (Sigma A2383) was present. In experiments with Rbin-1, Rbin-XL, or additional MIDAS protein present, 2% DMSO and 2 mM sodium sulfate were added to the assay buffer. Reaction velocities were determined by linear fitting to fluorescence time course data and dividing by the total Mdn1 concentration (25 nM). ATPase rates (V) as a function of ATP concentration (S) were fitted to the Michaelis-Menten equation:

$$V = \frac{k_{cat} \cdot [S]}{K_m + [S]}$$

Or the Hill equation:

$$V = \frac{k_{cat} \cdot [S]^h}{K_m^h + [S]^h}$$

where h reports the Hill coefficient. For Rbin and WT-MIDAS titrations, ATPase rates (V) were fitted to a dose-response equation:

$$V = \frac{A - b}{1 + \frac{[Rbin]}{EC_{50}}} + b$$

Where A reports the rate with no Rbin present and b reports the maximal inhibition (11). Fits were weighted by the inverse SEM. All data analysis and fitting were performed in MATLAB.

Rbin-XL Binding Assay. For Rbin-XL binding experiments, input protein (325 nM Mdn1-FL or Mdn1- Δ C or 1.5 μ M WT-MIDAS) was mixed with 0 μ M Rbin-XL (control lane), 2 μ M Rbin-XL (binding lane), or 2 μ M Rbin-XL + 50 μ M Rbin-1 (competition lane) in binding buffer (20 mM Hepes [pH 7.5], 150 mM NaCl, 1 mM MgCl₂, 3% wt/vol glycerol, 1 mM DTT, 0.01 μ M Mg-ATP, 2 mM NaSO₄, 0.1% Triton X-100, 0.05 mg/mL BSA) and incubated on ice in the dark for 30 min. Samples were then cross-linked using a 365-nm lamp (Spectroline ML-35005) for 120 s while on ice. Click reaction mix was then added to yield a final 10 mM Tris-hydroxypropyltriethylammonium chloride (Click Chemical Tools 1010), 4 mM CuSO₄ (Sigma 209198), 50 μ M 5-TAMRA azide (Click Chemical Tools 1245), and 100 mM sodium L-ascorbate (Sigma A4034). The click reaction was then run at 37 °C for 30 min in the dark. Samples were next run

on a Novex 4 to 20% Tris-Glycine gel (Thermo Fisher XP04205BOX). Rhodamine imaging was done using a Biorad ChemiDoc system, and Coomassie imaging was done using a LI-COR Odyssey system. Image analysis was done in ImageJ (National Institutes of Health; imagej.nih.gov/ij/). Details of Rbin-XL synthesis are in [SI Appendix, Supplemental Text](#).

Dynabead Pull-Down Assay. Mdn1- ΔC (65 nM) and biotinylated MIDAS protein (either WT-MIDAS or Δ Loop-MIDAS, 1 μ M unless otherwise stated) were incubated on ice (20 to 40 μ L initial reaction volume) for 30 min in binding buffer (20 mM Tris [pH 7.5], 150 mM NaCl, 1 mM MgCl₂, 0.5 mM EGTA, 1 mM DTT, 1 mM Mg-ATP, 2 mM NaSO₄, 0.05 mg/mL BSA, 0.002 to 0.02% Triton X-100, and 2% DMSO). MIDAS protein was left out for empty bead control. Rbin-1 was added at 1 μ M for example pull-downs and 0 to 50 μ M for the titration experiment. The reaction was then mixed with buffer-equilibrated Dynabeads M-280 streptavidin (Invitrogen 11205D) and incubated on ice for 30 min with mixing. The Dynabeads were separated with a magnet, and the supernatant was collected. The pellet was resuspended in SDS/PAGE loading buffer (50 mM Tris-HCl, 0.01% bromophenol blue, 6% glycerol, 100 mM DTT, 2% SDS) and boiled for 3 min for elution. Fractions were analyzed by SDS/PAGE on precast Novex 4 to 20% Tris-Glycine gels (Thermo Fisher XP04205BOX). Imaging was done using a LI-COR Odyssey system. All image analysis was done in ImageJ using the Gel tool to measure band intensities. For the WT-MIDAS titration experiment, data were fitted to a hyperbola:

$$f = \frac{[MIDAS] + [Mdn1\Delta C] + K_D - \sqrt{([MIDAS] + [Mdn1\Delta C] + K_D)^2 - 4 \cdot [Mdn1\Delta C] \cdot [MIDAS]}}{2 \cdot [Mdn1\Delta C]}$$

The fit was weighted by the inverse SEM at each data point.

Electron Microscopy Sample Preparation and Data Collection. A 3.5- μ L aliquot of purified Mdn1- ΔC + MIDAS sample at total 0.025 mg/mL (250 nM of nonbiotinylated SNAP-MIDAS and 25 nM of Mdn1- ΔC) was adsorbed for 1 min on a glow-discharged copper grid covered with a thin carbon film. The grid was blotted and washed two times with water before being stained with a 0.75% (wt/vol) uranyl formate solution as described (44). Specimens were imaged with a Philips CM10 electron microscope equipped with a tungsten filament and operated at an acceleration voltage of 100 kV. Micrographs were collected at a calibrated magnification of 41,513 \times (nominal magnification of 52,000 \times) with an XR16L-ActiveVu camera (AMT) at a defocus value of -1.5μ m.

Electron Microscopy Image Processing. For Mdn1- ΔC + WT-MIDAS, 13,335 particles were picked using the swarm option in EMAN2 (45) from 240 images and windowed into 200 \times 200-pixel images. Particle stacks were imported into RELION-3 (46), which was used for all subsequent image processing steps. After 2D classification, 10,189 particles from 9 classes were selected for initial model generation and subsequent 3D classification into 4 classes. The most populous class contained 8,253 particles and was subjected to supervised classification into 2 classes using a mask that only included the head domain with no image alignment. One reference map did not contain the MIDAS domain and yielded a density map from 5,530 particles at 20- \AA resolution. The second reference contained the MIDAS domain and yielded a density map from 2,723 particles at 21- \AA resolution. Difference map commands (vop resample and vop subtract), model docking, and figure generation were performed in UCSF Chimera (47). Maps were deposited to Electron Microscopy Data Bank (EMDB) in entries EMD-21911 and EMD-21912.

Native Mass Spectrometry (MS) Analysis. Protein samples were buffer-exchanged into native MS solution (NMSS; 150 mM ammonium acetate, pH 7.5, 0.01% Tween-20) using Zeba microspin desalting columns with a 40-kDa MWCO (48, 49). Nucleotides (Mg-ADP or AMP-PNP) were added to the protein sample at specific concentrations and incubated on ice for 30 min before or after buffer exchange. To assay for binding of Rbin-1, samples were buffer-exchanged into NMSS + 1% methanol and then incubated with varying concentrations of Rbin-1 on ice for 20 min prior to native MS analysis. For TEV-treated samples, incubation with TEV protease (Thermo Fisher Scientific) was performed on ice following the manufacturer-recommended protocol for 1 h prior to buffer exchange and native MS analysis.

Two to three microliters of the protein sample (1 to 2 μ M) was loaded into a gold-coated quartz emitter that was prepared in-house and then electrosprayed into an Exactive Plus EMR instrument (Thermo Fisher Scientific) with a static nanospray source (49). The MS settings include spray voltage, 1.0 to 1.4 kV; capillary temperature, 150 $^{\circ}$ C; in-source dissociation, 10 V; S-lens RF level, 200; resolving power, 17,500 at 200 Th; AGC target, 1 \times 10⁶; maximum injection time, 200 ms; number of microscans, 5; injection flat-tapole, 8 V; interflat-tapole, 4 V; bent flat-tapole, 4 V; in-source dissociation (ISD), 10 to 30 V; high energy collision dissociation (HCD), 200 V; ultrahigh vacuum pressure, 6 to 8 \times 10⁻¹⁰ mbar; and total number of scans, at least 100. Mass calibration in positive EMR mode was performed using cesium iodide solution. The acquired MS spectra were visualized using Thermo Xcalibur Qual Browser (version 3.0.63), and deconvolution was performed either manually or using UniDec version 3.2 (50, 51). The deconvolved spectra from UniDec were plotted using the *m/z* software (Proteometrics). Experimental masses were reported as the average mass \pm SD across all of the calculated mass values obtained within the observed charge state distribution.

Brownian Dynamics Modeling of Tethered MIDAS Domain. For modeling motion of the tethered MIDAS domain, the MIDAS domain was treated as a 4-nm-diameter sphere undergoing Brownian motion while tethered by D/E-rich region. The D/E-rich region was modeled as a worm-like chain (entropic spring) (52, 53), with the force-extension relationship:

$$F_{tether}(x) = \frac{k_B T}{4L_p} \left(\left(1 - \frac{x}{L_c} \right)^{-2} - \frac{1}{4} + \frac{x}{L_c} \right)$$

where k_B is the Boltzmann constant, T is absolute temperature, L_c is the contour length (188 nm for a 517-aa polypeptide), and L_p is the persistence length, estimated at 0.65 nm for an unstructured polypeptide (52–54). Motion of the tethered MIDAS domain was modeled using the overdamped Langevin equation:

$$-\gamma \frac{dx}{dt} + \sqrt{2DF_{therm}} = F_{tether}$$

where $\gamma = 6\pi\eta r$ is the drag coefficient of a sphere with radius r in fluid with viscosity η (set equal to the viscosity of water), D is the diffusion constant, and F_{therm} is a Gaussian white noise process with mean zero (55). This equation was integrated numerically using modified Euler's method, such that $x(t)$ was updated every 1-ns time step (Δt) by:

$$x_{n+1} = x_n + \sqrt{2D\Delta t}F_{therm} + \frac{1}{\gamma}F_{tether}\Delta t$$

The simulation was run for a total duration of 10 ms. The MIDAS docking site was approximated to be (x,y,z) = (6.28,0,22.96) nm away from the start of D/E-rich tether based on the cryo-EM structure of Mdn1-FL (9). Time spent within a 2-nm region was calculated by counting the number of 1-ns time steps spent in the region. All modeling was done in MATLAB.

Data Availability. Data for EM studies were deposited to the EMDB (EMD-21911 and EMD-21912).

ACKNOWLEDGMENTS. We thank members of the T.M.K. laboratory for useful discussions, Dr. Tommaso Cupido for help with NMR, Dr. Michael Miller for advice and coordination on chemical synthesis and inhibitor design, and Dr. Zhen Chen for initiating native MS work. T.M.K. is grateful to the National Institute of General Medical Sciences for funding (GM98579 and R35 GM130234-01). B.T.C. is grateful to the National Institute of General Medical Sciences for funding (P41 GM109824 and P41 GM103314). K.J.M. is supported by a National Cancer Institute K00 Fellowship (K00CA223018). The authors gratefully acknowledge the support generously provided by the Tri-Institutional Therapeutics Discovery Institute (TDI), a 501(c)(3) organization. TDI receives financial support from Takeda Pharmaceutical Company, TDI's parent institutes (Memorial Sloan Kettering Cancer Center, The Rockefeller University, and Weill Cornell Medicine), and a generous contribution from Mr. Lewis Sanders and other philanthropic sources. Molecular graphics and analyses were performed with UCSF Chimera, developed by the Resource for Bioinformatics, Visualization, and Informatics at the University of California, San Francisco, with support from NIH P41-GM103311.

1. A. F. Neuwald, L. Aravind, J. L. Spouge, E. V. Koonin, AAA+: A class of chaperone-like ATPases associated with the assembly, operation, and disassembly of protein complexes. *Genome Res.* 9, 27–43 (1999).
2. L. M. Iyer, D. D. Leippe, E. V. Koonin, L. Aravind, Evolutionary history and higher order classification of AAA+ ATPases. *J. Struct. Biol.* 146, 11–31 (2004).

3. A. N. Lupas, J. Martin, AAA proteins. *Curr. Opin. Struct. Biol.* 12, 746–753 (2002).
4. P. I. Hanson, S. W. Whiteheart, AAA+ proteins: Have engine, will work. *Nat. Rev. Mol. Cell Biol.* 6, 519–529 (2005).
5. J. P. Erzberger, J. M. Berger, Evolutionary relationships and structural mechanisms of AAA+ proteins. *Annu. Rev. Biophys. Biomol. Struct.* 35, 93–114 (2006).

6. R. T. Sauer *et al.*, Sculpting the proteome with AAA(+) proteases and disassembly machines. *Cell* **119**, 9–18 (2004).
7. J. E. Garbarino, I. R. Gibbons, Expression and genomic analysis of midasin, a novel and highly conserved AAA protein distantly related to dynein. *BMC Genomics* **3**, 18 (2002).
8. H. Schmidt, A. P. Carter, Review: Structure and mechanism of the dynein motor ATPase. *Biopolymers* **105**, 557–567 (2016).
9. Z. Chen *et al.*, Structural insights into Mdn1, an essential AAA protein required for ribosome biogenesis. *Cell* **175**, 822–834.e18 (2018).
10. P. Sosnowski *et al.*, The CryoEM structure of the *Saccharomyces cerevisiae* ribosome maturation factor Rea1. *eLife* **7**, e39163 (2018).
11. S. A. Kawashima *et al.*, Potent, reversible, and specific chemical inhibitors of eukaryotic ribosome biogenesis. *Cell* **167**, 512–524.e14 (2016).
12. Y. L. Ahmed, M. Thoms, V. Mitterer, I. Sinning, E. Hurt, Crystal structures of Rea1-MIDAS bound to its ribosome assembly factor ligands resembling integrin-ligand-type complexes. *Nat. Commun.* **10**, 3050 (2019).
13. D. Kressler, E. Hurt, H. Bergler, J. Bassler, The power of AAA-ATPases on the road of pre-60S ribosome maturation—Molecular machines that strip pre-ribosomal particles. *Biochim. Biophys. Acta* **1823**, 92–100 (2012).
14. E. M. Romes, M. Sobhany, R. E. Stanley, The crystal structure of the ubiquitin-like domain of ribosome assembly factor Ytm1 and characterization of its interaction with the AAA-ATPase midasin. *J. Biol. Chem.* **291**, 882–893 (2016).
15. C. Ulbrich *et al.*, Mechanochemical removal of ribosome biogenesis factors from nascent 60S ribosomal subunits. *Cell* **138**, 911–922 (2009).
16. C. Barrio-Garcia *et al.*, Architecture of the Rix1-Rea1 checkpoint machinery during pre-60S-ribosome remodeling. *Nat. Struct. Mol. Biol.* **23**, 37–44 (2016).
17. J. Bassler *et al.*, The AAA-ATPase Rea1 drives removal of biogenesis factors during multiple stages of 60S ribosome assembly. *Mol. Cell* **38**, 712–721 (2010).
18. S. Konikkat, J. L. Woolford Jr., Principles of 60S ribosomal subunit assembly emerging from recent studies in yeast. *Biochem. J.* **474**, 195–214 (2017).
19. T. Cupido, R. Pisa, M. E. Kelley, T. M. Kapoor, Designing a chemical inhibitor for the AAA protein spastin using active site mutations. *Nat. Chem. Biol.* **15**, 444–452 (2019).
20. G. L. Hersch, R. E. Burton, D. N. Bolon, T. A. Baker, R. T. Sauer, Asymmetric interactions of ATP with the AAA+ ClpX6 unfoldase: Allosteric control of a protein machine. *Cell* **121**, 1017–1027 (2005).
21. P. Rodriguez-Aliaga, L. Ramirez, F. Kim, C. Bustamante, A. Martin, Substrate-translocating loops regulate mechanochemical coupling and power production in AAA+ protease ClpXP. *Nat. Struct. Mol. Biol.* **23**, 974–981 (2016).
22. G. Bhabha *et al.*, Allosteric communication in the dynein motor domain. *Cell* **159**, 857–868 (2014).
23. H. Schmidt, E. S. Gleave, A. P. Carter, Insights into dynein motor domain function from a 3.3-Å crystal structure. *Nat. Struct. Mol. Biol.* **19**, 492–497, S1 (2012).
24. R. Z. Cer, U. Mudunuri, R. Stephens, F. J. Lebeda, IC50-to-Ki: A web-based tool for converting IC50 to Ki values for inhibitors of enzyme activity and ligand binding. *Nucleic Acids Res.* **37**, W441–W445 (2009).
25. C. Puchades *et al.*, Structure of the mitochondrial inner membrane AAA+ protease YME1 gives insight into substrate processing. *Science* **358**, eaao0464 (2017).
26. E. Zehr *et al.*, Katanin spiral and ring structures shed light on power stroke for microtubule severing. *Nat. Struct. Mol. Biol.* **24**, 717–725 (2017).
27. E. A. Zehr, A. Szyk, E. Szczesna, A. Roll-Mecak, Katanin grips the β -tubulin tail through an electropositive double spiral to sever microtubules. *Dev. Cell* **52**, 118–131.e6 (2020).
28. S. N. Gates, A. Martin, Stairway to translocation: AAA+ motor structures reveal the mechanisms of ATP-dependent substrate translocation. *Protein Sci.* **43**, 163 (2019).
29. T. Kon, M. Nishiura, R. Ohkura, Y. Y. Toyoshima, K. Sutoh, Distinct functions of nucleotide-binding/hydrolysis sites in the four AAA modules of cytoplasmic dynein. *Biochemistry* **43**, 11266–11274 (2004).
30. M. A. DeWitt, C. A. Cyranowska, F. B. Cleary, V. Bely, A. Yildiz, The AAA3 domain of cytoplasmic dynein acts as a switch to facilitate microtubule release. *Nat. Struct. Mol. Biol.* **22**, 73–80 (2015).
31. C. Cho, S. L. Reck-Peterson, R. D. Vale, Regulatory ATPase sites of cytoplasmic dynein affect processivity and force generation. *J. Biol. Chem.* **283**, 25839–25845 (2008).
32. Y.-C. C. Tsai *et al.*, Insights into the mechanism and regulation of the CbbQO-type rubisco activase, a MoxR AAA+ ATPase. *Proc. Natl. Acad. Sci. U.S.A.* **117**, 381–387 (2020).
33. Y.-C. C. Tsai, M. C. Lapina, S. Bhushan, O. Mueller-Cajar, Identification and characterization of multiple rubisco activases in chemoautotrophic bacteria. *Nat. Commun.* **6**, 8883 (2015).
34. M. Sutter *et al.*, Structural characterization of a newly identified component of α -carboxysomes: The AAA+ domain protein CsoCbbQ. *Sci. Rep.* **5**, 16243 (2015).
35. K. S. Wong, V. Bhandari, S. C. Janga, W. A. Houry, The RavA-ViaA chaperone-like system interacts with and modulates the activity of the fumarate reductase respiratory complex. *J. Mol. Biol.* **429**, 324–344 (2017).
36. M. N. Fodje *et al.*, Interplay between an AAA module and an integrin I domain may regulate the function of magnesium chelatase. *J. Mol. Biol.* **311**, 111–122 (2001).
37. J. Snider, W. A. Houry, MoxR AAA+ ATPases: A novel family of molecular chaperones? *J. Struct. Biol.* **156**, 200–209 (2006).
38. J. Snider *et al.*, Formation of a distinctive complex between the inducible bacterial lysine decarboxylase and a novel AAA+ ATPase. *J. Biol. Chem.* **281**, 1532–1546 (2006).
39. M. Luo *et al.*, Characterization of the novel protein KIAA0564 (Von Willebrand domain-containing protein 8). *Biochem. Biophys. Res. Commun.* **487**, 545–551 (2017).
40. D. L. Coy, W. O. Hancock, M. Wagenbach, J. Howard, Kinesin's tail domain is an inhibitory regulator of the motor domain. *Nat. Cell Biol.* **1**, 288–292 (1999).
41. H. Y. K. Kaan, D. D. Hackney, F. Kozielski, The structure of the kinesin-1 motor-tail complex reveals the mechanism of autoinhibition. *Science* **333**, 883–885 (2011).
42. R. J. McKenney, W. Huynh, M. E. Tanenbaum, G. Bhabha, R. D. Vale, Activation of cytoplasmic dynein motility by dynactin-cargo adapter complexes. *Science* **345**, 337–341 (2014).
43. S. R. Hubbard, Autoinhibitory mechanisms in receptor tyrosine kinases. *Front. Biosci.* **7**, d330–d340 (2002).
44. M. Ohi, Y. Li, Y. Cheng, T. Walz, Negative staining and image classification—Powerful tools in modern electron microscopy. *Biol. Proced. Online* **6**, 23–34 (2004).
45. G. Tang *et al.*, EMAN2: An extensible image processing suite for electron microscopy. *J. Struct. Biol.* **157**, 38–46 (2007).
46. J. Zivanov *et al.*, New tools for automated high-resolution cryo-EM structure determination in RELION-3. *eLife* **7**, e42166 (2018).
47. E. F. Pettersen *et al.*, UCSF Chimera—A visualization system for exploratory research and analysis. *J. Comput. Chem.* **25**, 1605–1612 (2004).
48. P. D. B. Olinares *et al.*, A robust workflow for native mass spectrometric analysis of affinity-isolated endogenous protein assemblies. *Anal. Chem.* **88**, 2799–2807 (2016).
49. P. D. B. Olinares, B. T. Chait, Native mass spectrometry analysis of affinity-captured endogenous yeast RNA exosome complexes. *Methods Mol. Biol.* **2062**, 357–382 (2020).
50. M. T. Marty *et al.*, Bayesian deconvolution of mass and ion mobility spectra: From binary interactions to polydisperse ensembles. *Anal. Chem.* **87**, 4370–4376 (2015).
51. D. J. Reid *et al.*, MetaUniDec: High-Throughput deconvolution of native mass spectra. *J. Am. Soc. Mass Spectrom.* **30**, 118–127 (2019).
52. M. S. Kellermayer, S. B. Smith, H. L. Granzier, C. Bustamante, Folding-unfolding transitions in single titin molecules characterized with laser tweezers. *Science* **276**, 1112–1116 (1997).
53. M. L. Kutys, J. Fricks, W. O. Hancock, Monte Carlo analysis of neck linker extension in kinesin molecular motors. *PLoS Comput. Biol.* **6**, e1000980 (2010).
54. L. J. Lapidus, P. J. Steinbach, W. A. Eaton, A. Szabo, J. Hofrichter, Effects of chain stiffness on the dynamics of loop formation in polypeptides. Appendix: Testing a 1-dimensional diffusion model for peptide dynamics. *J. Phys. Chem. B* **106**, 11628–11640 (2002).
55. K. J. Mickolajczyk, A. S. I. Cook, J. P. Jevtha, J. Fricks, W. O. Hancock, Insights into kinesin-1 stepping from simulations and tracking of gold nanoparticle-labeled motors. *Biophys. J.* **117**, 331–345 (2019).